Compositional diversity of near-, far-side transitory zone around Naonobu, Webb and Sinus Successus craters: Inferences from Chandrayaan-1 Moon Mineralogy Mapper (M^3) data

Rishikesh Bharti, D Ramakrishnan* and K D Singh

Department of Earth Sciences, Indian Institute of Technology, Bombay, Powai 400 076, Mumbai, India.
**Corresponding author. e-mail: ramakrish@iitb.ac.in*

This study investigated the potential of Moon Mineralogy Mapper (M^3) data for studying compositional variation in the near-, far-side transition zone of the lunar surface. For this purpose, the radiance values of the M^3 data were corrected for illumination and emission related effects and converted to apparent reflectance. Dimensionality of the calibrated reflectance image cube was reduced using Independent Component Analysis (ICA) and endmembers were extracted by using Pixel Purity Index (PPI) algorithm. The selected endmembers were linearly unmixed and resolved for mineralogy using United States Geological Survey (USGS) library spectra of minerals. These mineralogically resolved endmembers were used to map the compositional variability within, and outside craters using Spectral Angle Mapper (SAM) algorithm. Cross validation for certain litho types was attempted using band ratios like Optical Maturity (OMAT), Color Ratio Composite and Integrated Band Depth ratio (IBD). The identified lithologies for highland and basin areas match well with published works and strongly support depth related magmatic differentiation. Prevalence of pigeonite-basalt, pigeonite-norite and pyroxenite in crater peaks and floors are unique to the investigated area and are attributed to local, lateral compositional variability in magma composition due to pressure, temperature, and rate of cooling.

1. Introduction

Several planetary scientists consider the Moon as an endmember among the planetary bodies of our solar system (Hiesinger and Head-III 2006). In recent years, considerable efforts have been made to enhance the existing understanding about Moon–Earth system. Since 1990, several space missions have been launched for expanding our knowledge and understanding about lunar topography, composition, internal structure, and magnetic field. The remotely sensed information and samples collected from the lunar surface are invaluable and have broadened our understanding of the physical and chemical properties of the Earth–Moon system (Hiesinger and Head-III 2006). The mineral composition of the Moon surfaces contain vital clues about its thermo-chemical evolution (Staid *et al.* 2010). The complexity of the lunar crustal composition, both spatially and depthwise, is manifested in numerous ways (Dhingra *et al.* 2011) like changes in crustal thickness in the near-, and far-side (Wieczorek and Phillips 1998), varied lithological composition

Keywords. Imaging spectroscopy; Moon Mineralogy Mapper (M^3); Naonobu crater; planetary exploration; spectral deconvolution.

of crater central peaks (Tompkins *et al.* 1999), and geographically concentrated occurrence of lithologies such as KREEP (Lawrence *et al.* 2000). These variations are attributable to processes like magma ocean formation and solidification, differentiation and overturn, large scale convection, and volcanic activity (Lucey *et al.* 2006; Taylor *et al.* 2009). Salient among the rock types reported on the lunar surface include Anorthosite, low Plagioclase Gabbroic-Noritic-Troctolitic Anorthosite, high Plagioclase Gabbroic-Noritic-Troctolitic Anorthosite, Anorthositic Norite, Anorthositic Gabbro-Norite, Anorthositic Gabbro, Norite, Gabbro-Norite, Gabbro, and Anorthositic Troctolite. These rock types characterize the Feldspathic Highlands Terrane (FHT), Procellarum KREEP Terrane (PKT), and South Pole-Aitken (SPA) Terrane (Jolliff *et al.* 2000; Korotev 2000). These changes in mineralogy on lunar surface can be deciphered from the reflectance/emission spectra

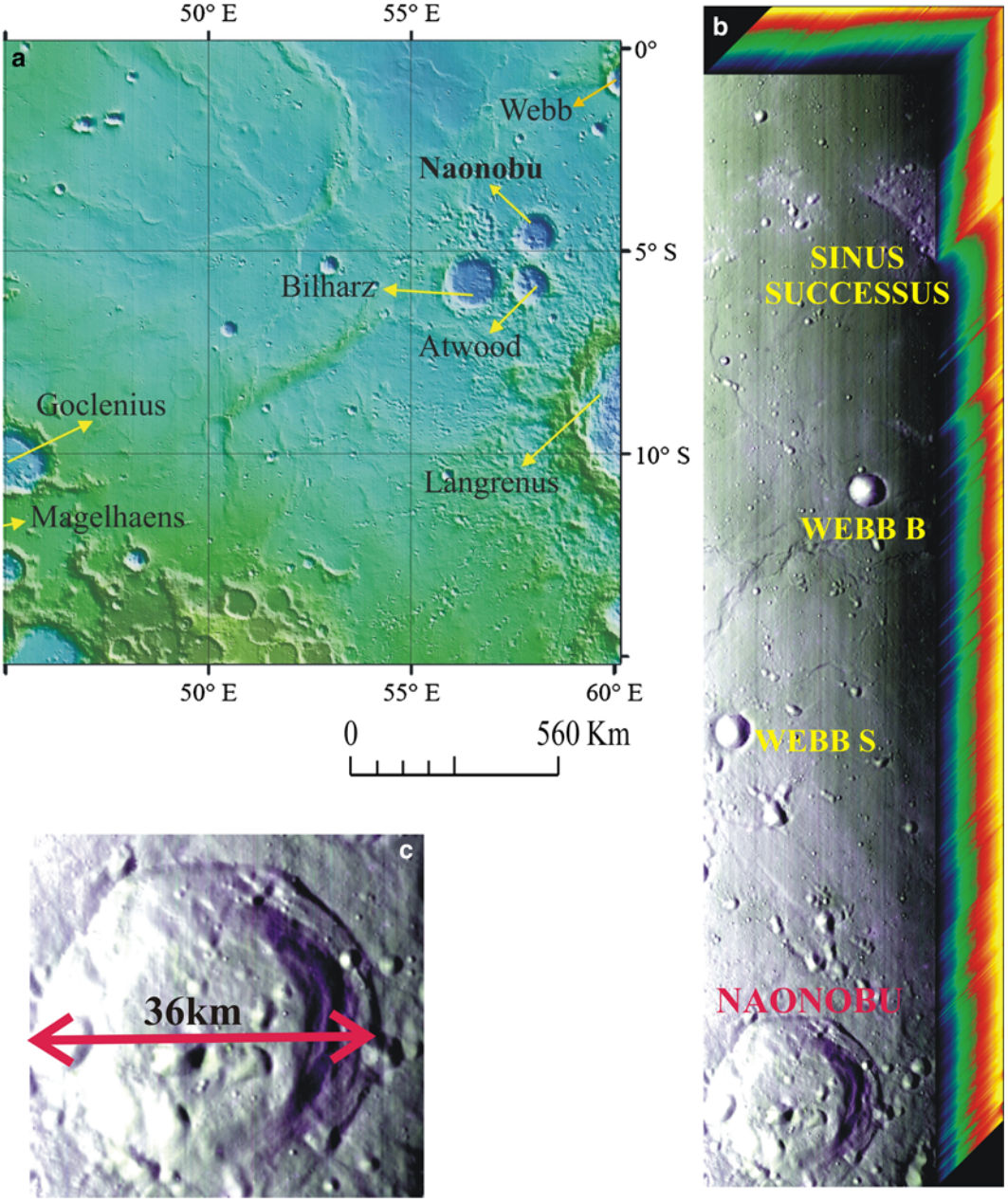

Figure 1. (**a**) Identified Naonobu crater region with surrounding craters like Atwood, Bilharz, Langrenus and Webb are marked in Clementine (UVVIS) topographic data. (**b**) Extent of the study area represented by a hypercube (Band_81, Band_83 and Band_85) of M^3 data. Naonobu crater is falling in lower portion of the image. (**c**) Enlarged view of Naonobu crater.

with diagnostic absorption features at characteristic wavelengths. The position, shape, depth, and width of these absorption features are governed by chemical composition and atomic structure and can be directly related to mineralogy (Hunt and Salisbury 1970; van der Meer and De Jong 2006). This ability of spectroscopy is being exploited by the remote sensing community in exploring the Earth and planetary surfaces for more than three decades (Goetz *et al.* 1985; Boardman and Huntington 1996; Mustard *et al.* 1998; Crosta and Filho 2000; Vaughan *et al.* 2003; Crouvi *et al.* 2006; van der Meer *et al.* 2006; Nowicki and Christensen 2007; Rogers and Christensen 2007; Galvo *et al.* 2008; Ramakrishnan and Kusuma 2008; Besse *et al.* 2011; Pour and Hashim 2011, 2012).

Till recently, multispectral orbiters (e.g., Clementine) have been the main source of understanding the compositional variability of the lunar surface. Though these data have high spatial resolution, they had limited spectral resolution to resolve subtle changes in absorption positions representing different minerals (Kramer *et al.* 2011a). However, 'the release of new, global imaging spectrometer data from the Moon Mineralogy Mapper (M^3) onboard Chandrayaan-1 marks the passing of the torch to the next generation of lunar spectroscopy and new understanding of the Moon' (Kramer *et al.* 2011a). M^3, developed by Brown University records the reflected radiations from lunar surface in 85 spectral bands (global mode) between 0.46 and 2.9 μm wavelength range of electromagnetic radiation with a spatial resolution of 140 m (Pieters *et al.* 2009). The wavelength range (0.46–2.9 μm) covered by this instrument allows to map the crystal field absorptions for quantitative mineralogical mapping (Klima *et al.* 2011). M^3 datasets are found to be of immense use in Moon exploration such as structure and crustal mineralogical studies of lunar surface (Kramer *et al.* 2011a), study of Marius Hills complex (Besse *et al.* 2011), compositional analyses of olivine-rich areas (Isaacson *et al.* 2011), Mg-spinel bearing central peaks (Dhingra *et al.* 2011), low Ca-pyroxene on lunar surfaces (Klima *et al.* 2011) and optical maturation and hydroxyl ion formation (Kramer *et al.* 2011b). However, detailed understanding on the upper-, and lower-lunar crust is still a gap area and warrants further research (Dhingra *et al.* 2011).

In this study, the changes in composition of the lunar surface around Naonobu, Webb B, Webb S and Sinus Successus crater (figure 1) is investigated. Since the study area falls in transitory zone between low- and high-lands, the mineralogical variability is expected to be maximum and hence, has the potential to shed light on the compositional variability between upper- and lower-lunar crust.

2. Materials and methodology

2.1 *The Moon Mineralogy Mapper* (M^3)

The M^3 data records the reflected radiance from the Moon's surface in pushbroom mode between 0.46 and 2.97 μm in 85 contiguous spectral bands. In this study, 12-bit quantized global mode data is used which has 140 m spatial resolution (Pieters *et al.* 2009). The preprocessing of M^3 data involves spectral radiance calibration, dark signal subtraction, bad detector element correction, detector array tap interpolation, filter seam interpolation, electronic panel ghost correction, dark pedestal shift correction, scattered light correction, flat field correction, radiometric calibration, and ray tracing and pixel location (L1B data manual). The spectra collected by M^3 sensor in 0.46–2.97 μm wavelength region of the electromagnetic spectrum have the potential to identify most of the silicate and other group of minerals. The absorption spectral feature such as central wavelength, depth and Full Width Half Maximum (FWHM) permit the image to be resolved for mineralogy and abundances.

2.2 M^3 *data calibration*

The first step in M^3 data calibration involves conversion of radiance values to apparent reflectance using equation (1) (Clark 1979; Clark *et al.* 2011).

$$R'_\lambda = \pi \times d^2 \times L_{\mathrm{rad}(\lambda)}/F_{\mathrm{sun}(\lambda)} \times \cos(\theta) \times P \quad (1)$$

where,

θ	Solar zenith angle,
R'_λ	Apparent reflectance,
P	Phase function correction (unavailable),
d	Distance from the Sun to the Moon (AU),
$L_{\mathrm{rad}(\lambda)}$	Radiance value measured by M^3 sensor as a function of wavelength,
$F_{\mathrm{sun}(\lambda)}$	Exo-atmospheric solar spectral irradiances as a function of wavelength.

From the blackbody reflectance curve (figure 2) it is evident that beyond 2 μm wavelength range, reflectance spectra are a mixture of reflection and thermal emission and hence, the pixel spectra of M^3 data will have higher radiance at longer wavelengths. With increase in temperature, the effect of thermal emission increases and significantly affects the reflectance spectra. Clark (1979) and Clark

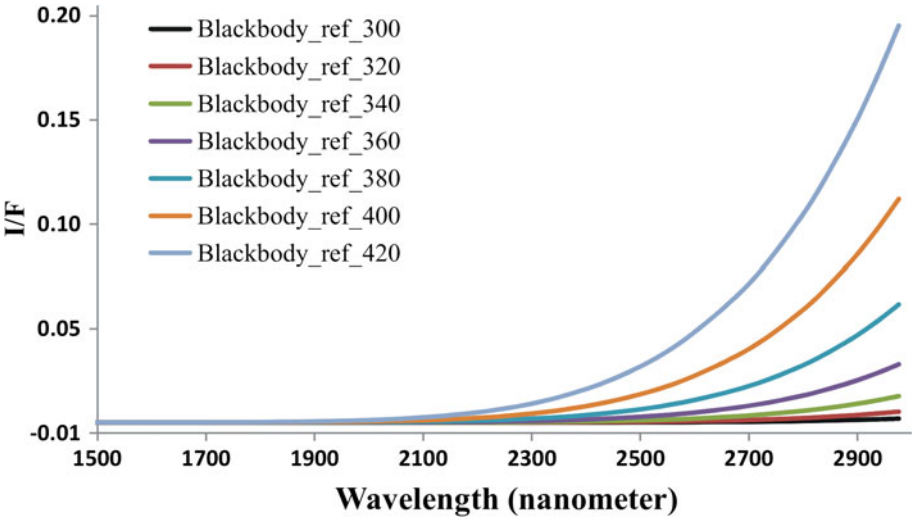

Figure 2. Calculated apparent reflectance (I/F) of blackbody using Planck's blackbody radiance at different temperature (300–420 K) with exo-atmospheric solar irradiance at 1 AU. There is significant effect of thermal emission in longer wavelength (>2000 nm) whereas in the shorter wavelengths the effect is almost negligible. The effect of temperature increases as the temperature of the blackbody increases.

et al. (2011) have addressed this problem and laid down the procedure for removing the thermal emission component. Based on albedo variability in the M^3 image, representative locations (T1, T2, T3, ..., T6) were selected (figure 3) to estimate the brightness temperature. Subsequently, lunar surface temperature was estimated by matching the image spectra with blackbody radiance spectra (figure 4) at different temperatures. Then, emission component for each pixel is corrected by adjusting the image radiance to the blackbody radiance at the estimated average temperature.

2.3 *M^3 data analysis*

Akin to processing any hypercube, the M^3 data also needs to be corrected for coherent and non-coherent noises and high-dimensionality. Traditionally, Principal Components Analysis (PCA) and the Maximum Noise Fraction (MNF) are widely used to reduce dimensionality in hyperspectral remote sensing (Wang and Chang 2006). However, in recent times Independent Component Analysis (ICA) is extensively preferred over PCA and MNF due to its efficacy in signal separation. In this study, we performed ICA to reduce the data and noise. Once the hypercube is corrected for noise, spectrally unique pixels, endmembers (EM) need to be extracted from the image to resolve the in scene spectral variability (Chang *et al.* 2006; Plaza *et al.* 2006). In this study, the Pixel Purity Index (PPI) algorithm (Boardman 1994) embedded in ENVI software was used to identify the compositionally unique endmember spectra from the M^3 data. The adopted sequence of data processing is given below as a flow chart.

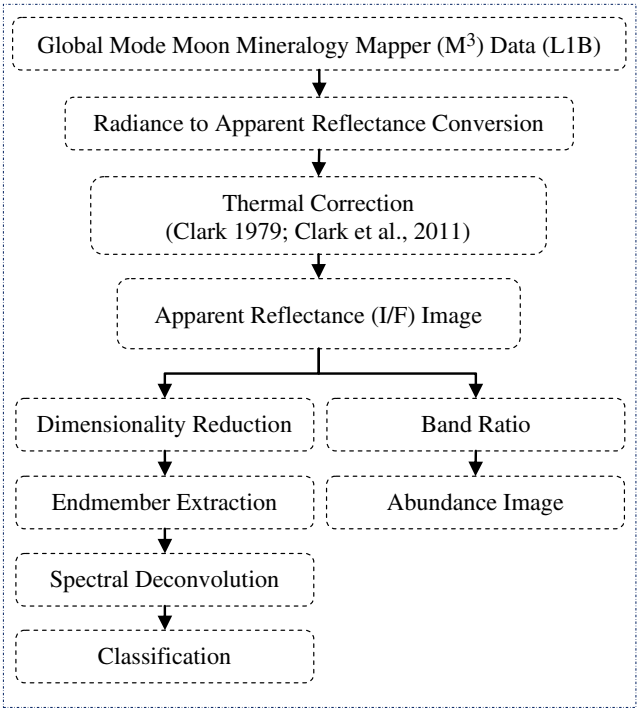

Since the image derived endmember represents a large footprint (140 m) on the Moon's surface, the pixel spectra is often a mixture of several rock types with unique constituent minerals. Therefore, each pixel spectra of M^3 image need to be unmixed to know the constituent minerals (figure 5). In this study, a fully constrained Linear Mixing Model

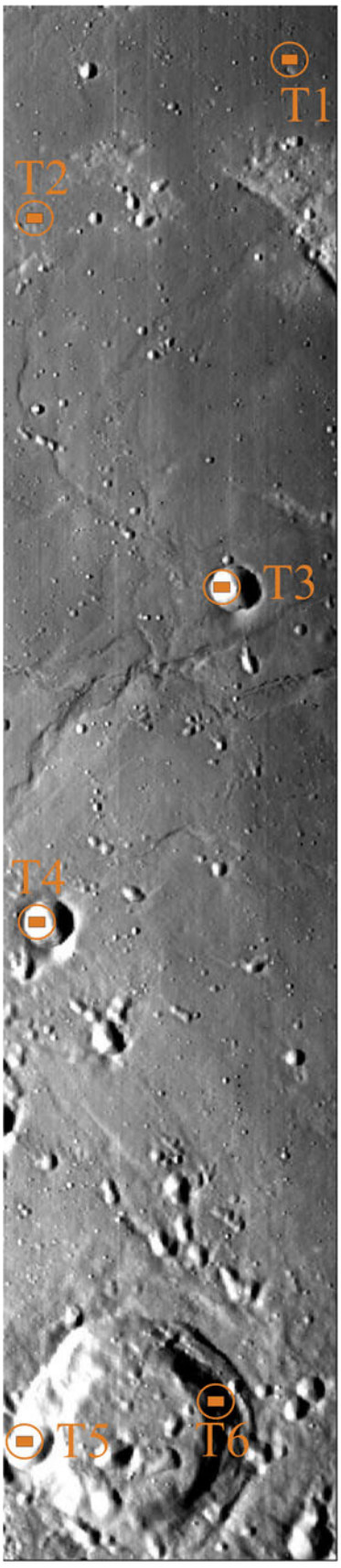

Figure 3. T1, T2, T3, T4, T5 and T6 are the test sites used to derive the thermal emission component in apparent reflectance spectra.

(LMM) (equation 2) was used to identify the minerals and their abundances (Mustard and Sunshine 1999). This iterative, least square approach (Heinz and Chang 2001; Yang *et al.* 2009) resolves each one of the M^3 endmembers for constitutive mineralogy based on least Root Mean Square Error (RMSE) (equation 3). For this purpose, mineral spectra from the United States Geological Survey (USGS) and Jet Propulsion Laboratory (JPL) spectral libraries were used. Pearson Correlation Coefficient (PCC) (Xiong *et al.* 2004) was adopted to identify the potential mineral spectra (from library). PCC inherently addresses the similarities in absorption feature such as central wavelength, FWHM, and depth of absorption.

$$x = \arg\min_{x} \|Mx - r\|_2^2 + \beta \left\| \sum_{i=1}^{q} x_i - 1 \right\|_2^2 + \gamma \left\| \sum_{i=1}^{q} \text{sign}\,(x_i)^T x_i - 1 \right\|_2^2, \quad (2)$$

where x is the abundance of image derived endmember r ($r_i \in \Re^{n\times 1}$), $M \in \Re^{n\times q}$ is the matrix of selected candidates from spectral repository (USGS), n is the number of wavelength channel in input spectra (endmember and library) and q is the number of endmembers. The estimated abundances satisfy the positivity and sum-to-unity constraints, as Legendre coefficients β and γ.

$$\text{RMSE} = \sqrt{\frac{\sum_{i=1}^{n} \eta\,(\lambda)_i^2}{n}},$$

where

$$\eta = \sum_{i=1}^{n} |r_i - M_i| \quad (3)$$

where $\eta_i \sim N_n\,(0, \sigma^2 I_n)$ is the vector of errors. Here, N_n represents the n-variable multivariate-normal distribution with error variance σ^2, 0 is an $n \times 1$ vector of zeroes, and I_n is the identity matrix of order n.

Besides the spectral similarity based approach to discriminate the mineralogy, band ratios at critical wavelengths (e.g., 1/2 μm; 0.42/0.75 μm) were also attempted to delineate the specific mineral abundances such as olivine and spinel. This approach helps to ascertain the results achieved by SAM (Isaacson *et al.* 2011).

3. Results

3.1 *Analyses of endmember spectra*

Each endmember retrieved by PPI was linearly unmixed and the abundances of constituent library

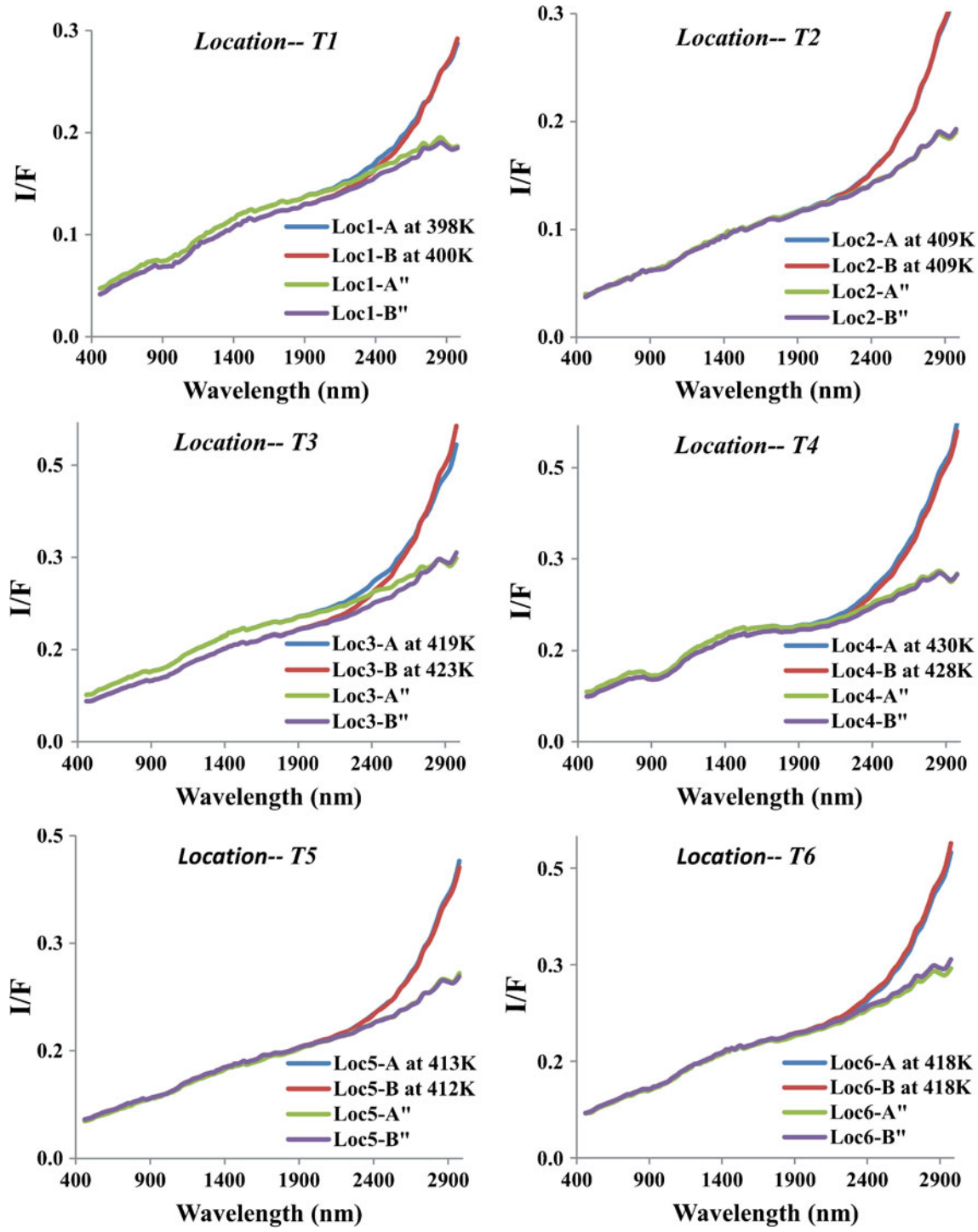

Figure 4. Spectral plots represent the pixel and thermal emission removed spectra from test sites (T1, T2, T3, . . ., T6). In the above figures, legend with quotation marks (") represent the thermal emission component removed apparent reflectance spectra.

minerals were estimated (table 1; figures 6 and 7). In the investigated area, eight major rock types and several variants within them are observed. The major rock types include basalt, olivine-basalt, pigeonite-basalt, high Fe-basalt, norite, pigeonite-norite, anorthosite, and pyroxenite. The variants are discriminated by the preponderance of the constituent minerals such as pigeonite, olivine, hypersthene and type of plagioclase.

The basaltic rocks (EM-7) contains clinopyroxene (10–24%), plagioclase (40–75%) with subordinate amount of hypersthene (3–10%) and iron

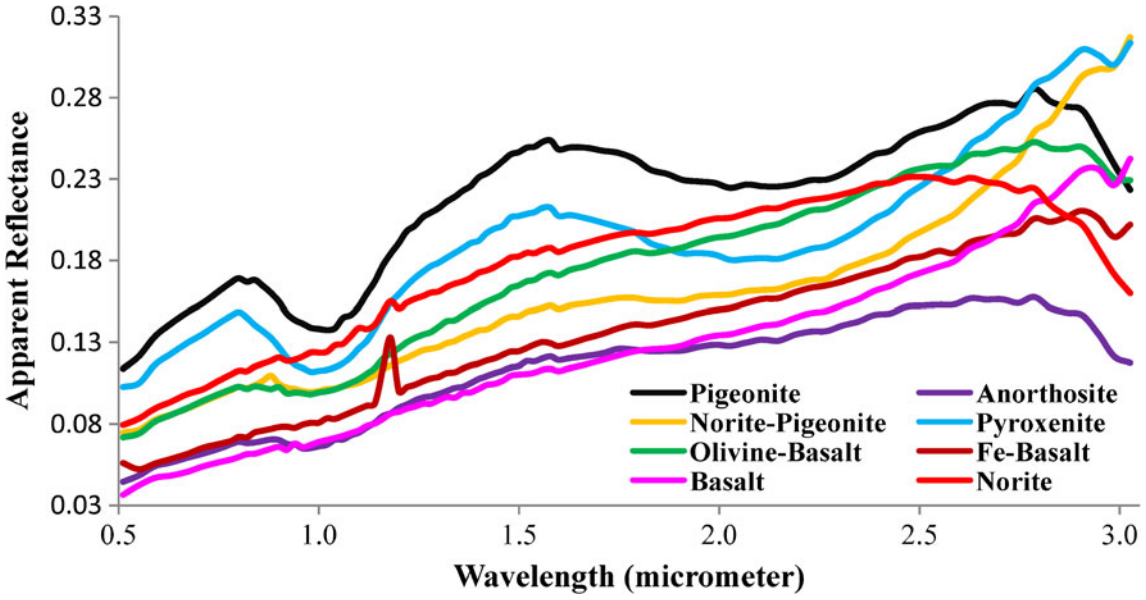

Figure 5. Image derived endmembers (pure pixel spectra).

Table 1. *Mineralogical composition and matching error of the best matching spectra.*

Image derived endmembers	Mineralogical composition (%) of the best matched library modelled spectra	SAM score	RMSE
Endmember-1 (Pigeonite-basalt)	Augite (9–37), Pigeonite (32–57), Albite (9–51), Hypersthene (1–13), Anorthite (7), Olivine (1), Magnetite (5–8)	0.989	0.001
Endmember-2 (Anorthosite)	Augite (2–24), Albite (35–88), Magnetite (5–9), Hypersthene (2–14), Anorthite (7), Pigeonite (2), Olivine (10)	0.991	0.001
Endmember-3 (Norite)	Augite (9–15), Anorthite (26–63), Olivine (1), Albite (52), Magnetite (9–10), Hypersthene (4–12)	0.990	0.001
Endmember-4 (Pigeonite-norite)	Augite (6–33), Pigeonite (14–56), Albite (19–77), Magnetite (2–8), Hypersthene (3–12), Olivine (1)	0.990	0.001
Endmember-5 (Pyroxenite)	Augite (44), Pigeonite (31), Magnetite (4), Hypersthene (21)	0.980	0.002
Endmember-6 (Olivine-basalt)	Augite (18), Diopside (2), Olivine (19), Albite (47), Magnetite (7), Hypersthene (8)	0.991	0.001
Endmember-7 (basalt)	Augite (9), Pigeonite (1), Albite (83), Magnetite (2), Hypersthene (6)	0.987	0.001
Endmember-8 (Fe-basalt)	Augite (4), Anorthite (28), Diopside (20), Olivine (8), Magnetite (39), Fassaite (1)	0.958	0.004

(5–8%). In case of olivine basalts (EM-6), the percentage of olivine ranges from 18–20%. The anorthosites (EM-2) are dominated by labradorite plagioclase (80–88%) with subordinate amounts of mafic minerals such as pyroxene (3–6%) and iron (2–8%). The pigeonite-basalt (EM-1) contains significant proportions of pigeonite (30–50%) in addition to other basaltic constituents. Basalts with near equal proportions of pigeonite (13–15%) and hypersthene (11–16%) are termed as pigeonite-norite (EM-4). The norites (EM-3) are characterized by 10–11% of hypersthenes and are devoid of pigeonite. In this study, we have come across certain anomalous regions characterized by high percentage of pyroxenes [augite (40–44%), pigeonite (25–31%), hypersthenes (15–21%)] with minor amounts of iron (3–5%). These rocks are designated as lunar pyroxenite (EM-5).

3.2 *Spatial mapping of lithotypes*

To know the spatial distribution of the above rock types, Spectral Angle Mapper (SAM) algorithm

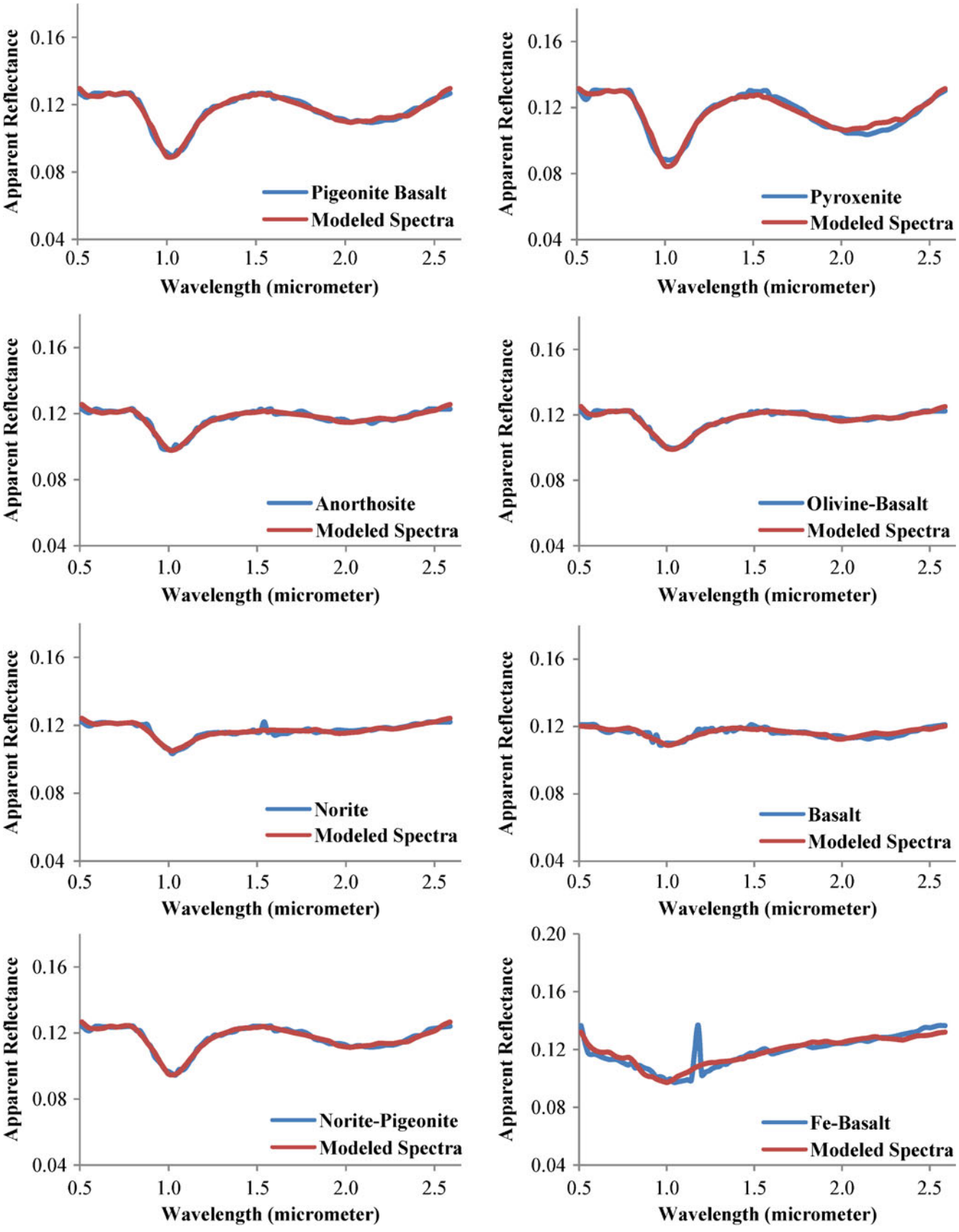

Figure 6. Plots represent the image derived endmembers with their best matching linearly modelled (library) spectra.

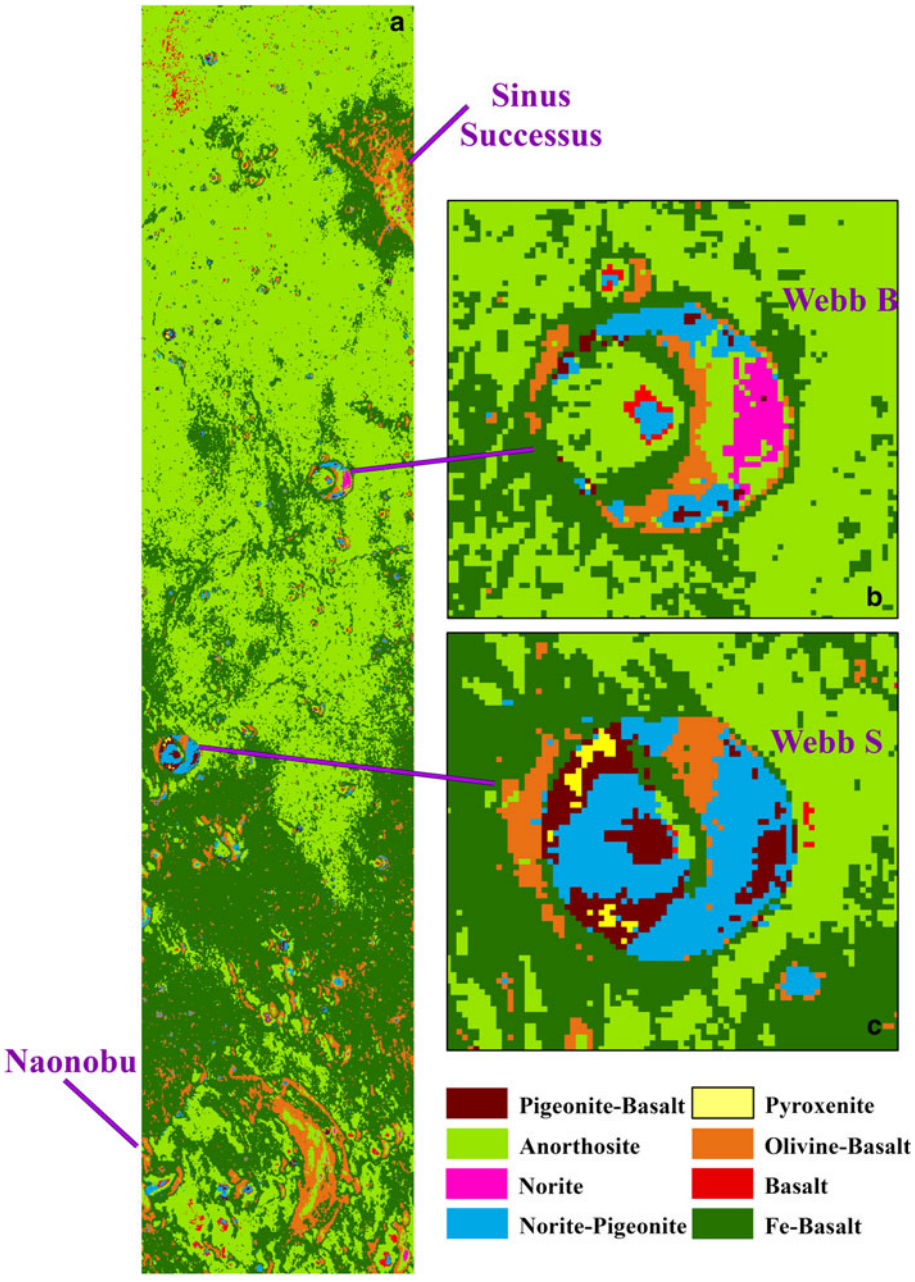

Figure 7. M^3 classified (SAM) image with image-derived endmembers.

(equation 4) was used. The SAM algorithm classifies the pixels based on the similarity between the reference (endmember/field/library) and unknown (pixel) spectra. SAM measures the angle between target and reference spectra and assigns the target pixel to a particular class based on the threshold provided by the user (Kruse *et al.* 1993; Dennison *et al.* 2004). The SAM score approaching 1 point to perfect match and 0 to no match.

$$\alpha = \cos^{-1}\left[\frac{\sum_{i=1}^{nb} t_i r_i}{\left(\sum_{i=1}^{nb} t_i^2\right)^{\frac{1}{2}}\left(\sum_{i=1}^{nb} r_i^2\right)^{\frac{1}{2}}}\right] \qquad (4)$$

where nb is the number of bands, t_i is the target spectrum (pixel), and r_i is the reference spectra (library).

In this study, we considered a threshold of 0.80 to map the different rock types in the M^3 image. From the figure it is evident that the inter-crater area is characterized by two major rock types, namely anorthosite (with featureless spectra) and Fe-basalt. Spatial transition from basalt, Fe-basalt and olivine-basalt is observed in the northwestern parts (figure 7) of the area. Most of the lithological variations could be seen within the crater and crater rim areas (figure 7b, c). The crater floor depth in this area varied from 3360 (Naonobu) to

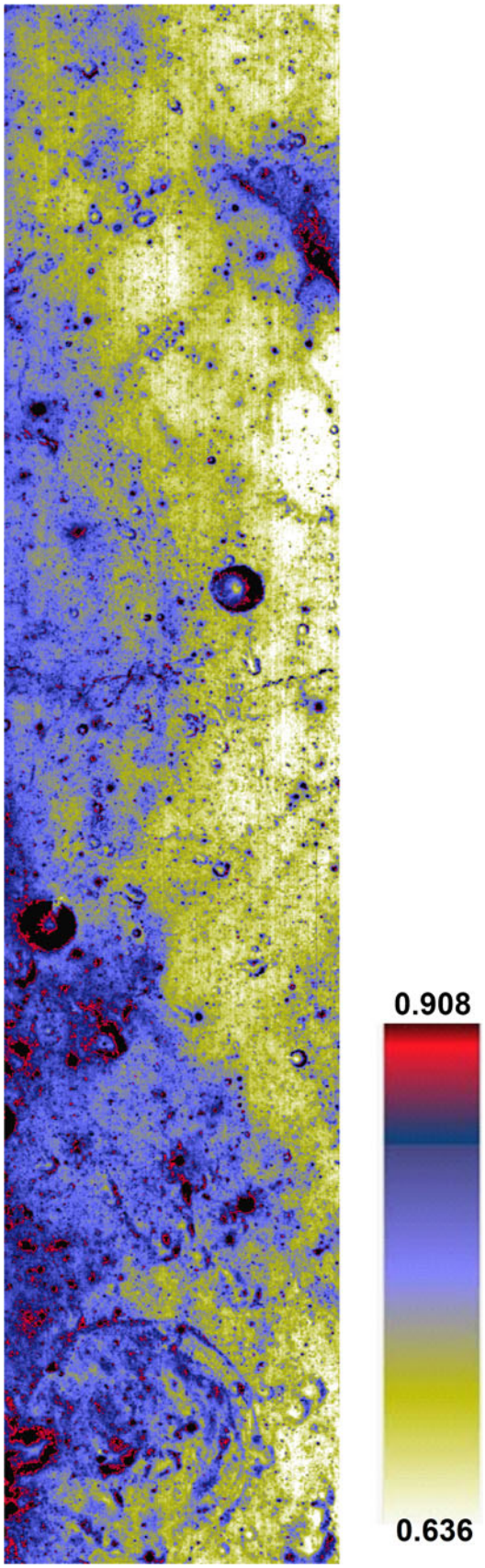

Figure 8. The ratio of integrated 1 and 2 μm band depths; high values represent olivine-rich areas.

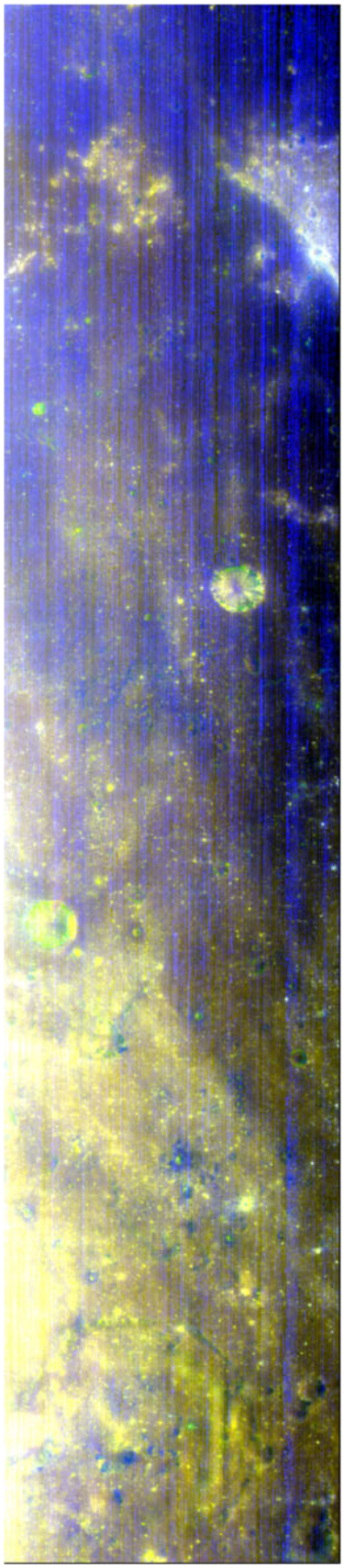

Figure 9. RGB display of three integrated band depths (Red: sum of 0.79–1.3 μm; Green: sum of 1.6–2.5 μm and Blue: sum of 0.42–0.75 μm). The light yellow–green colour confirms the presence of pyroxenes.

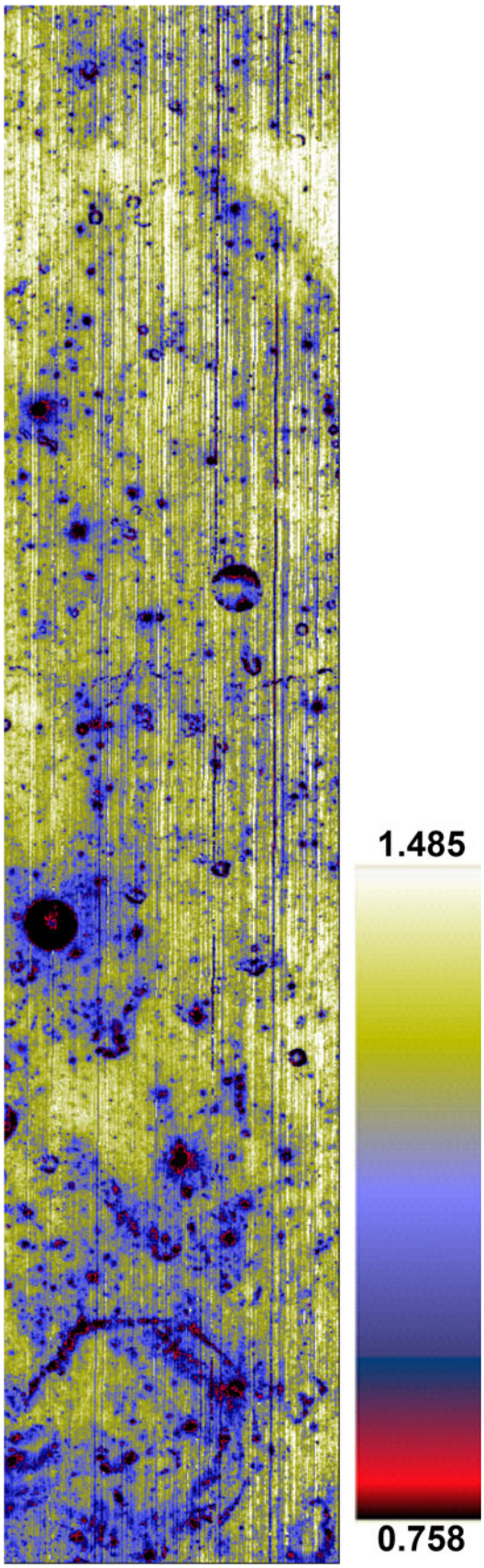

Figure 10. Optical Maturity (OMAT). Higher value of OMAT represents unweathered surface.

2000 m (Webb B) from the surface. The central ridges of the crater are observed to have pigeonite-basalt/pigeonite-norite. These rocks have transitional contacts with olivine-basalt, basalt and Fe-basalt, representing the depthwise changes in composition.

Integrated Band Depth (IBD) ratio of 1 and 2 μm has been used to identify the olivine spatial distribution around Naonobu crater area (figure 8). The high value of band ratio image represents the olivine distribution in the study area. Naonobu craters as well as adjacent craters show a high value, which confirms the presence of olivine. Colour ratio composites have integrated 2 μm band depth in red, integrated 1μm band depth in green and 0.64/0.75 μm in blue, shown in figure 9. The area surrounding Naonobu crater appears in light yellow–green colour which confirms the presence of pyroxenes. Optical Maturity (OMAT) has also been studied using ratio of 0.94–0.74 μm (figure 10) which shows the degree of maturity and relates to the exposure age of the surface. Higher value of OMAT represents unweathered surface whereas lower OMAT value represents weathered surface. The OMAT spectral ratio is controlled by both composition and maturity.

4. Discussion and conclusions

Mapping the spatial and depthwise compositional variability of the lunar crust has been one of the most challenging tasks for the planetary exploration community. Every time a new technology is implemented in lunar orbiter/lander or rover, new findings and understandings emerge. This speaks about the unknown aspects of the lunar surface and interior. In this light, the hyperspectral payload, M^3, onboard Chandrayaan-1 mission has shed some critical information on large scale mineralogical- and lithological-variations that could not be unraveled by earlier lunar orbiters (Taylor 1982; Demidova *et al.* 2007; Isaacson *et al.* 2011). One such observation is the discovery of spinel-rich deposits on the lunar surface (Pieters *et al.* 2009, 2010, 2011; Dhingra *et al.* 2011; Lal *et al.* 2012). Identification of several such areas on the rim of Moscoviense basin indicates that Mg–Al spinel rich areas contain less than 5% mafic silicate minerals (olivine and pyroxene). Pieters *et al.* (2011) suggested that these deposits represent a previously unknown lunar rock type, a spinel anorthosite, which might be an important component of the lunar crust. Another important and recent understanding on the Moon mineralogy is identification of regions of quartz, silica-rich glass, and alkali feldspar (Glotch *et al.* 2010). The spectral character of these areas is distinct from

surrounding mare, highlands, and regions comprising anorthosites (Bhattacharya *et al.* 2011). These areas also form a variety of landforms and suggest that both extrusive and intrusive silicic magmatism occurred on the Moon.

The above two findings distinctly indicate magmatic differentiation process (Wieczorek *et al.* 2006; Ariskin 2007; Glotch *et al.* 2010). Two basic models are proposed to account for the presence of such highly evolved compositions on the Moon. Firstly, silicate liquid immiscibility mechanism is proposed for the origin of granite/felsite composition (Jolliff *et al.* 1999). To develop such rocks, basaltic magma has to undergo nearly complete fractional crystallization before the single residual melt separates into two immiscible melts, one that is SiO_2-poor and FeO-rich, and one that is rich in SiO_2 and alkalis. It is unlikely that the silicic lavas produced from the small amount of residual melt could form large volcanic structures such as the Gruithuisen Domes or Hansteen Alpha (Hagerty *et al.* 2006). The second possible mechanism that could produce large volumes of silicic melt is basaltic underplating, in which a hot basaltic magma intrudes into the lunar crust, causing melting of the anorthositic crust and the generation of silicic magmas (Hagerty *et al.* 2006). In both cases, it is expected to have compositional variability suggestive of either or both processes.

This study aimed at delineating the compositional variability in a transitory zone between near-, and far-side of the Moon using the M^3 data and hyperspectral image processing flow chain. Besides the Mare basalts and high land anorthosites, we recorded a suite of compositionally related basic rocks. These include pyroxenite, norite, olivine-basalt, high Fe-basalt, pigeonite-basalt and pigeonite-norite. It is evident from figure 7 that the pigeonite-basalt and pigeonite-norite typically constitute the central peaks of craters of Webb-S, and -B, whereas, the floor of Naonobu (3360 m deep) is made of basic rocks (olivine-basalt and Fe-basalt). Compositions of central peaks, crater wall and floors are considered very important as they reflect composition of uplifted material originating from varying depths of the lunar crustal column. Typically, highlands crater peaks are consistent with gabbroic, noritic, or troctolitic-anorthosite compositions. Peaks of craters in or around basins are mostly composed of anorthositic-norite and a wider range of gabbroic, noritic, or troctolitic-anorthosites (Tompkins *et al.* 1999). Recently, Dhingra *et al.* (2011) reported Mg-spinel rich crater peaks. Such depth-related compositional variability in craters and central peaks is possible only if magmatic differentiation exists. In addition, lateral compositional inconsistency is possible within a certain range of depth due to the effects of local pressure and temperature on differentiation. Such conditions can favour lateral lithological changes. In the investigated area, pigeonite bearing rocks (pigeonite-basalt and pigeonite-norite) and pyroxenite are observed in the crater central peaks and floors. Such rocks are not reported ubiquitously. As pigeonite can be preserved only in fast cooling systems, their presence can be directly related to magma composition and rate of cooling.

Following points emerge from this study:

- Calibrated and corrected M^3 data in conjunction with LMM is useful to resolve the compositional variability of the investigated area.
- The mapped lithological variations arrived at by LMM agree with the existing understanding on the composition of highlands and basins.
- Magmatic differentiation is mainly responsible for changes in depthwise composition. However, for a given depth, lateral compositional variability is possible due to differential pressure–temperature related effects. Presence of diversified lithologies like pigeonite-basalt, pigeonite-norite, olivine-basalt, pyroxenite within craters of comparable depth supports the above fact.

Acknowledgements

Authors acknowledge NASA Discovery Program, Science Mission Directorate (http://ode.rsl.wustl.edu/moon/) for sharing the M^3 data free of cost. DR acknowledges the critical comments from the reviewers that helped to improve the quality of the paper.

References

Ariskin A A 2007 Parental magmas of lunar troctolites: Genetic problems and estimated original compositions; *Geochem. Int.* **45(5)** 413–427.

Besse S, Sunshine J M, Staid M I, Petro N E, Boardman J W, Green R O, Head J W, Isaacson P J, Mustard J F and Pieters C M 2011 Compositional variability of the Marius Hills volcanic complex from the Moon Mineralogy Mapper (M^3); *J. Geophys. Res.* **116** E00G13.

Bhattacharya S, Chauhan P, Rajawat A S and Kiran Kumar A S 2011 Lithological mapping of central part of Mare Moscoviense using Chandrayaan-1 Hyperspectral Imager (HySI) data; *ICARUS* **212(2)** 470–479.

Boardman J W 1994 Geometric mixture analysis of imaging spectrometery data; *Proc. Int. Geosci. Remote Sens. Symp.* **4** 2369–2371.

Boardman J W and Huntington J H 1996 Mineral mapping with AVIRIS data; In: *Summaries of the 6th Annual JPL Airborne Earth Science Workshop* (Pasadena, California: JPL Publication) 96 **4(1)** 9–11.

Chang C I, Wu C, Liu W and Ouyang Y 2006 A new growing method for simplex-based endmember extraction algorithm; *IEEE Trans. Geosci. Remote Sens.* **44(10)** 2804–2819.

Clark R N 1979 Planetary reflectance measurements in the region of planetary thermal emission; *ICARUS* **40** 94–103.

Clark R N, Pieters C M, Green R O, Boardman J W and Petro N E 2011 Thermal removal from near-infrared imaging spectroscopy data of the Moon; *J. Geophys. Res.* **116** E00G16.

Crosta A P and Filho C R S 2000 Hyperspectral remote sensing for mineral mapping: A case-study at Alto Paraiso De Goias, Central Brazil; *Rev. Brasil. Geosci.* **30(3)** 551–554.

Crouvi O, Ben-Dor E, Beyth M, Avigad D and Amit R 2006 Quantitative mapping of arid alluvial fan surfaces using field spectrometer and hyperspectral remote sensing; *Rem. Sens. Environ.* **104** 103–117.

Demidova S I, Nazarov M A, Lorenz C A, Kurat G, Brandstätter F and Ntaflos Th 2007 Chemical composition of lunar meteorites and the lunar crust; *Petrology* **15(4)** 386–407.

Dennison P E, Halligan K Q and Roberts D A 2004 A comparison of error metrics and constraints for multiple endmember spectral mixture analysis and spectral angle mapper; *Remote Sens. Environ.* **93(3)** 359–367.

Dhingra D, Pieters C M, Boardman J W, Head III J W, Isaacson P J, Taylor L A and the M^3 Team 2011 Theophilus crater: Compositional diversity and geological context of Mg-spinel bearing central peaks; *Lunar Planet. Sci. Conf., XLII*, abstract 2388.

Galvo S G, Formaggio A R, Couto E G and Roberts D A 2008 Relationships between the mineralogical and chemical composition of tropical soils and topography from hyperspectral remote sensing data; *J. Photogram. Rem. Sens.* **63** 259–271.

Glotch T D, Lucey P G, Bandfield J L, Greenhagen B T, Thomas I R, Elphic R C, Bowles N, Wyatt M B, Allen C C, Hanna K D and Paige D A 2010 Highly silica compositions on the Moon; *Science* **329** 1510–1513.

Goetz A F H, Vane G, Solomon J E and Rock B N 1985 Imaging spectrometry for earth; *Rem. Sens. Sci.* **228** 1147–1153.

Hagerty J J, Lawrence D J, Hawke B R, Vaniman D T, Elphic R C and Feldman W C 2006 Refined thorium abundances for lunar red spots: Implications for evolved, non-mare volcanism on the Moon; *J. Geophys. Res.* **111** E06002.

Heinz D C and Chang C 2001 Fully constrained least squares linear spectral mixture analysis method for material quantification in hyperspectral imagery; *IEEE Trans. Geosci. Remote Sens.* **39(3)** 529–545.

Hiesinger H and Head-III J W 2006 New views of lunar geosciences: An introduction and overview; *Rev. Mineral. Geochem.* **60** 1–81.

Hunt G R and Salisbury J W 1970 Visible and near infrared spectra of minerals and rocks: I. Silicate minerals; *Mod. Geol.* **1** 283–300.

Isaacson P J, Pieters C M, Besse S, Clark R N, Head J W, Klima R L, Mustard J F, Petro N E, Staid M I, Sunshine J M, Taylor L A, Thaisen K G and Tompkins S 2011 Remote compositional analysis of lunar olivine-rich lithologies with Moon Mineralogy Mapper (M^3) spectra; *J. Geophys. Res.* **116** E00G11.

Jolliff B L, Loss C F, McCallum I S and Chwartz J M S 1999 Geochemistry, petrology, and cooling history of 14161,7373: A plutonic lunar sample with textural evidence of granitic-fraction separation by silicate-liquid immiscibility; *Am. Mineral.* **84** 821–837.

Jolliff B L, Gillis J J, Haskin L A, Korotev R L and Wieczorek M A 2000 Major lunar crustal terranes: Surface expressions and crust-mantle origins; *J. Geophys. Res.* **105** 4197–4416.

Klima R L, Pieters C M, Boardman J W, Green R O, Head-III J W, Isaacson P J, Mustard J F, Nettles J W, Petro N E, Staid M I, Sunshine J M, Taylor L A and Tompkins S 2011 New insights into lunar petrology: Distribution and composition of prominent low-Ca pyroxene exposures as observed by the Moon Mineralogy Mapper (M^3); *J. Geophys. Res.* **116** E00G06.

Korotev R L 2000 The great lunar hotspot and the composition and origin of the Apollo mafic (LKFM) impact-melt breccias; *J. Geophys. Res.* **105** 4317–4345.

Kramer G Y, Besse S, Nettles N, Combe J P, Clark R N, Pieters C M, Staid M, Malaret E, Boardman J, Green R O, Head J W and McCord T B 2011a Newer views of the Moon: Comparing spectra from Clementine and the Moon Mineralogy Mapper; *J. Geophys. Res.* **116** E00G04.

Kramer G Y, Besse S, Dhingra D, Nettles J W, Klima R L, Garrick-Bethell I, Clark R N, Combe J P, Head III J W, Taylor L A, Pieters C M, Boardman J and McCord T B 2011b M^3 spectral analysis of lunar swirls and the link between optical maturation and surface hydroxyl formation at magnetic anomalies; *J. Geophys. Res.* **116** E00G18.

Kruse F A, Lefkoff A B, Boardman J W, Heidebrecht K B, Shapiro A T, Barloon P J and Goetz A F H 1993 The Spectral Image Processing System (SIPS) interactive visualization and analysis of imaging spectrometer data; *Remote Sens. Environ.* **44** 145–163.

Lal D, Chauhan P, Shah R D, Bhattacharya S, Ajai and Kiran Kumar A S 2012 Detection of Mg spinel lithologies on central peak of crater Theophilus using Moon Mineralogy Mapper (M^3) data from Chandrayaan-1; *J. Earth Syst. Sci.* **121(3)** 847–853.

Lawrence D J, Feldman W C, Barraclough B L, Binder A B, Elphic R C, Maurice S, Miller M C and Prettyman T H 2000 Thorium abundances on the lunar surface; *J. Geophys. Res.* **105(E8)** 20,307–20,331.

Lucey P, Korotev R L, Gillis J J, Taylor L A, Lawrence D, Elphic R, Feldman B, Hood L L, Hunten D, Mendillo M, Noble S, Papike J J and Reedy R C 2006 Chapter 2. Understanding the lunar surface and space–moon interactions; In: New Views of the Moon, *Rev. Mineral. Geochem.* **60** 83–219.

Mustard J F, Li L and He G 1998 Nonlinear spectral mixture modeling of lunar multispectral data: Implications for lateral transport; *J. Geophys. Res.-Planets* **103** 419–425.

Mustard J F and Sunshine J M 1999 Spectral analysis for earth science: Investigations using remote sensing data; In: *Manual of remote sensing* (eds) Rencz A and Ryerson R A, 3rd edn (New York: John Wiley and Sons), 286p.

Nowicki S A and Christensen P R 2007 Rock abundance on Mars from the thermal emission spectrometer; *J. Geophys. Res.* **112** E05007 1–20.

Pieters C M, Boardman J, Buratti B, Chatterjee A, Clark R, Glavich T, Green R, Head-III J, Isaacson P, Malaret E, McCord T, Mustard J, Petro N, Runyon C, Staid M, Sunshine J, Taylor L, Tompkins S, Varanasi P and White M 2009 The Moon Mineralogy Mapper (M^3) on Chandrayaan-1; *Curr. Sci.* **96(4)** 500–505.

Pieters C M, Boardman J, Buratti B, Clark R, Combe J P, Green R, Goswami J N, Head J W, Hicks M, Isaacson P, Klima R, Kramer G, Kumar K, Lundeen S, Malaret E, McCord T B, Mustard J, Nettles J, Petro N, Runyon C, Staid M, Sunshine J, Taylor L A, Thaisen K, Tompkins S and Varanasi P 2010 Identification of a new spinel-rich lunar rock type by the Moon Mineralogy Mapper (M^3); *41st Lunar Planet. Sci. Conf., Woodlands, Texas*, 1854p.

Pieters C M, Besse S, Boardman J, Buratti B, Cheek L, Clark R N, Combe J P, Dhingra D, Goswami J N, Green

R O, Head J W, Isaacson P, Klima R, Kramer G, Lundeen S, Malaret E, McCord T, Mustard J, Nettles J, Petro N, Runyon C, Staid M, Sunshine J, Taylor L A, Thaisen K, Tompkins S and Whitten J 2011 Mg-spinel lithology: A new rock type on the lunar farside; *J. Geophys. Res.* **116** E00G08.

Plaza A, Valencia D, Plaza J and Chang C 2006 Parallel implementation of endmember extraction algorithms from hyperspectral data; *IEEE Geosci. Remote Sens. Lett.* **3(3)** 334–338.

Pour B A and Hashim M 2011 Identification of hydrothermal alteration minerals for exploring of porphyry copper deposit using ASTER data, SE Iran; *J. Asian Earth Sci.* **42** 1309–1323.

Pour B A and Hashim M 2012 Identifying areas of high economic-potential copper mineralization using ASTER data in Urumieh–Dokhtar Volcanic Belt, Iran; *Adv. Space Res.* **49** 753–769.

Ramakrishnan D and Kusuma K N 2008 Marine clays and its impact on the rapid urbanization developments: A case study of Mumbai area using EO-1-Hyperion data; In: *Hyperspectral remote sensing and spectral signature applications* (ed.) Rajendran S (New Delhi: New India Publishing Agency), pp. 53–64.

Rogers A D and Christensen P R 2007 Surface mineralogy of Martian low-albedo regions from MGS-TES data: Implications for upper crustal evolution and surface alteration; *J. Geophys. Res.* **112** E01003 1–18.

Staid M I, Pieters C M, Boardman J, Head J W, Sunshine J, Taylor L A, Isaacson P, Besse S, Klima R, Kramer G and Dhingra D 2010 Regional and temporal variations in the western mare basalts: New observations from the Moon Mineralogy Mapper; *41st Lunar and Planetary Science Conference.*

Taylor S R 1982 Planetary science: A lunar perspective; Lunar and Planetary Institute, USA, 481p.

Taylor L A, Liu Y, Pieters C M, Tompkins S, Isaacson P J, Cheek L and Thaisen K 2009 Lunar magma ocean crust: Implications of FeO contents in plagioclase; *Lunar Planet. Sci. Conf., XL*, abstract 1304.

Tompkins S, Hawke B R and Pieters C M 1999 Distribution of materials within the crater Tycho: Evidence for large gabbroic bodies in the highlands; *Lunar Planet. Sci. Conf. XXX*, Houston, TX, LPI.

van der Meer F and De Jong S 2006 Imaging spectrometry: Basic principles and prospective applications (The Netherlands: Springer Publishers), 451p.

van der Meer F, Yang H and Lang H 2006 Imaging spectrometery and geological applications; In: Imaging spectrometry: Basic principles and perspective applications (The Netherlands: Springer Publishers), pp. 201–218.

Vaughan R G, Calvin W M and Taranik J V 2003 SEBASS hyperspectral thermal infrared data: Surface emissivity measurement and mineral mapping; *Rem. Sens. Environ.* **85** 48–63.

Wang J and Chang C I 2006 Independent component analysis-based dimensionality reduction with applications in hyperspectral image analysis; *IEEE Trans. Geosci. Remote Sens.* **44(6)** 1586–1600.

Wieczorek M A, Jolliff B L, Khan A, Pritchard M E, Weiss M P, Williams J G, Hood L L, Righter K, Neal C R, Shearer C K, McCallum I S, Tompkins S, Hawke B R, Peterson C, Gillis J J and Bussey B 2006 Constitution and structure of the Moon; *Rev. Mineral. Geochem.* **60** 221–364.

Wieczorek M A and Phillips R J 1998 Potential anomalies on a sphere: Applications to the thickness of the lunar crust; *J. Geophys. Res.* **103** 1715–1724.

Xiong H, Shekhar S, Tan P N and Kumar V 2004 Exploiting a support-based upper bound of Pearson's Correlation Coefficient for efficiently identifying strongly correlated pairs; *ACM SIGKDD*, Seattle, WA, USA.

Yang Z, Farison J and Thompson M 2009 Fully constrained least squares estimation of target quantifications in hyperspectral images; *Proc. IPCV*, pp. 910–915.

MS received 8 November 2012; revised 30 April 2013; accepted 1 June 2013